

Pericoronary adipose tissue feature analysis in computed tomography calcium score images in comparison to coronary computed tomography angiography

Yingnan Song,^a Hao Wu,^a Juhwan Lee^{ORCID},^a Justin Kim^{ORCID},^a Ammar Hoori^{ORCID},^a Tao Hu,^a Vladislav Zimin,^b Mohamed Makhlof,^b Sadeer Al-Kindi,^c Sanjay Rajagopalan,^b Chun-Ho Yun,^d Chung-Lieh Hung,^e and David L. Wilson^{ORCID},^{a,f,*}

^aCase Western Reserve University, Department of Biomedical Engineering, Cleveland, Ohio, United States

^bUniversity Hospitals Cleveland Medical Center, Harrington Heart and Vascular Institute, Cleveland, Ohio, United States

^cHouston Methodist, Center for Computational and Precision Health, DeBaakey Heart and Vascular Center, Houston, Texas, United States

^dMacKay Memorial Hospital, Division of Radiology, Department of Internal Medicine, Taipei, Taiwan

^eMacKay Memorial Hospital, Division of Cardiology, Department of Internal Medicine, Taipei, Taiwan

^fCase Western Reserve University, Department of Radiology, Cleveland, Ohio, United States

ABSTRACT. **Purpose:** We investigated the feasibility and advantages of using non-contrast CT calcium score (CTCS) images to assess pericoronary adipose tissue (PCAT) and its association with major adverse cardiovascular events (MACE). PCAT features from coronary computed tomography angiography (CCTA) have been shown to be associated with cardiovascular risk but are potentially confounded by iodine. If PCAT in CTCS images can be similarly analyzed, it would avoid this issue and enable its inclusion in formal risk assessment from readily available, low-cost CTCS images.

Approach: To identify coronaries in CTCS images that have subtle visual evidence of vessels, we registered CTCS with paired CCTA images having coronary labels. We developed an “axial-disk” method giving regions for analyzing PCAT features in three main coronary arteries. We analyzed hand-crafted and radiomic features using univariate and multivariate logistic regression prediction of MACE and compared results against those from CCTA.

Results: Registration accuracy was sufficient to enable the identification of PCAT regions in CTCS images. Motion or beam hardening artifacts were often prevalent in “high-contrast” CCTA but not CTCS. Mean HU and volume were increased in both CTCS and CCTA for the MACE group. There were significant positive correlations between some CTCS and CCTA features, suggesting that similar characteristics were obtained. Using hand-crafted/radiomics from CTCS and CCTA, AUCs were 0.83/0.79 and 0.83/0.77, respectively, whereas Agatston gave AUC = 0.73.

Conclusions: Preliminarily, PCAT features can be assessed from three main coronary arteries in non-contrast CTCS images with performance characteristics that are at the very least comparable to CCTA.

© The Authors. Published by SPIE under a Creative Commons Attribution 4.0 International License. Distribution or reproduction of this work in whole or in part requires full attribution of the original publication, including its DOI. [DOI: [10.1117/1.JMI.12.1.014503](https://doi.org/10.1117/1.JMI.12.1.014503)]

Keywords: computed tomography calcium score; pericoronary adipose tissue; coronary artery disease; risk prediction; radiomic; machine learning

Paper 24326GR received Oct. 19, 2024; revised Dec. 30, 2024; accepted Jan. 3, 2025; published Jan. 24, 2025.

*Address all correspondence to David L. Wilson, david.wilson@case.edu

1 Introduction

Low-cost CTCS images provide an opportunity to assess cardiovascular health beyond the traditional Agatston calcification score. Agatston score and other assessments of calcifications, including our own calcium-omics approach, are predictors of major adverse cardiovascular events (MACE).¹⁻⁴ In these images, it is also possible to opportunistically assess fat depots (e.g., epicardial and liver fat) that have been shown to be also predictors of MACE.⁵ Recently, there has been a notable focus on pericoronary adipose tissue (PCAT) as assessed in coronary computed tomography angiography (CCTA) images as a risk factor for MACE. In this report, we opportunistically assess PCAT features from non-contrast CTCS images and use them singly and together to determine their role in MACE prediction.

A variety of pathways have been suggested where PCAT inflammation may be involved in local stimulation of atherosclerotic plaque formation.^{6,7} The “outside-in” theory implicates inflamed adipocytes in PCAT in the production of adipocytokines which through its effects on adventitia lead to atherosclerosis.⁸ Fat depots with high lipid content have lower attenuation in CT, whereas more aqueous adipose tissues have a higher HU value than adipose tissue.⁹ Fat attenuation index, a metric related to CCTA mean HU values in a 3D distribution of tissue around the coronary artery region has been linked to inflammation using biopsy samples taken from patients undergoing cardiac surgery.¹⁰ CCTA-based radiomic profiling of coronary artery PCAT detects perivascular structural remodeling associated with coronary artery disease (CAD) and improves cardiovascular risk prediction.^{11,12}

Regarding CCTA analysis of PCAT, the variable presence of iodine could be a confound, especially regarding average HU values and the size of PCAT volume. Recent studies have shown that the impact of iodine contrast in CCTA PCAT assessment is demonstrated as increased HU value, leading to false positive of fat inflammation detection.¹³ Our group investigated dynamic PCAT enhancement in cardiac CT perfusion studies.¹⁴ The presence of iodine can confound HU attenuation, volume, and radiomic features, all of which can further depend on the timing of the CCTA acquisition and the presence of obstructive disease. This suggests that there might be an advantage to using CTCS images to assess PCAT. The absence of a contrast agent avoids these complications in CCTA images.

In this report, we analyzed PCAT features in non-contrast CTCS images and assessed their role in MACE prediction. The use of CTCS images presents an advantage as there are exceptionally large cohorts of low-cost CTCS images, enabling big data analysis for machine learning. However, CTCS images also present challenges—the lack of an iodine contrast agent to identify the coronaries and thick slice (3-mm thick) images complicating some standard processing such as curved planar reformatting. In this study, we created new methods for extracting PCAT features from left anterior descending artery (LAD), left circumflex artery (LCX), and right coronary artery (RCA) arteries in CTCS images, extracted features, compared results with those from CCTA images, and determined the role of CTCS PCAT on MACE prediction.

2 Methods

2.1 Data Acquisition

This study was approved as a retrospective study of de-identified images by our local institutional review board in Mackay Memorial Hospital, Taiwan. Images have been acquired from 2013 to 2018 at Mackay Memorial Hospital, Taiwan, and shared under a data use agreement. The population consisted of 83 consecutive patients with suspected CAD who underwent both CTCS (120 kVp, 30 mAs, 3-mm slice thickness) from a dual source scanner (Siemens SOMATOM) and CCTA (100 kVp, 600 mAs, 0.75-mm slice thickness Definition Flash). CCTA and CTCS pairs were obtained in the same imaging session with CTCS obtained 5 min prior to any contrast injection. The exclusion criteria for the patients were (1) age < 20 years, (2) coronary artery bypass grafting, (3) acute or old myocardial infarction, (4) complete left bundle branch block, and (5) inadequate datasets such as poor image quality of CCTA, which may arise due to factors such as patient motion, improper contrast enhancement, or suboptimal scanner settings. Of the 83 patients, 14 had a MACE outcome, which was defined as cardiovascular death, acute myocardium infarction or revascularization. CTCS Agatston score was calculated using the

Table 1 Characteristics of paired CCTA and CTCS studies.

Variable	Mean (count)	Std (%)
Age	58.0	12.3
Gender: male	56	67
Calcium score	213.8	561.9
Diabetic	17	20
Hypertension	51	61
Satin use	33	39
Aspirin use	26	31

conventional detection criteria (three connected voxels >130 HU) and summed to give a total score. Population characteristics are shown in Table 1.

2.2 Image Processing and Feature Extraction from PCAT

The processing pipeline is described in Fig. 1. To analyze PCAT in paired CCTA and non-contrast CTCS images, several image processing steps were performed. Using the CCTA images with ready visualization of coronary arteries, two cardiology fellows specializing in cardiovascular imaging semi-automatically segmented and identified the centerlines of the three main coronary arteries (LAD, LCX, and RCA), using commercial software (Intuition Client version 4.4.13.P7, TeraRecon, Inc.). Each image was initially processed by one resident, and the accuracy of the segmentation was subsequently verified by another person to ensure quality and consistency. Because coronaries are poorly visible in non-contrast CTCS images, we registered CCTA (floating image volume) to CTCS (reference image volume) to identify the coronaries. We used the Deeds non-rigid registration method,¹⁵ a 3D registration technique that uses a minimum spanning tree approach to find a global optimum. This method has been found to be robust to “sliding” organs, a desirable attribute for heart registration. Prior to registration, we sampled CCTA images to be the same size as CTCS images and windowed the HU range of both CCTA and CTCS images (-300 HU, 300 HU) to give better contrast for the coronary artery

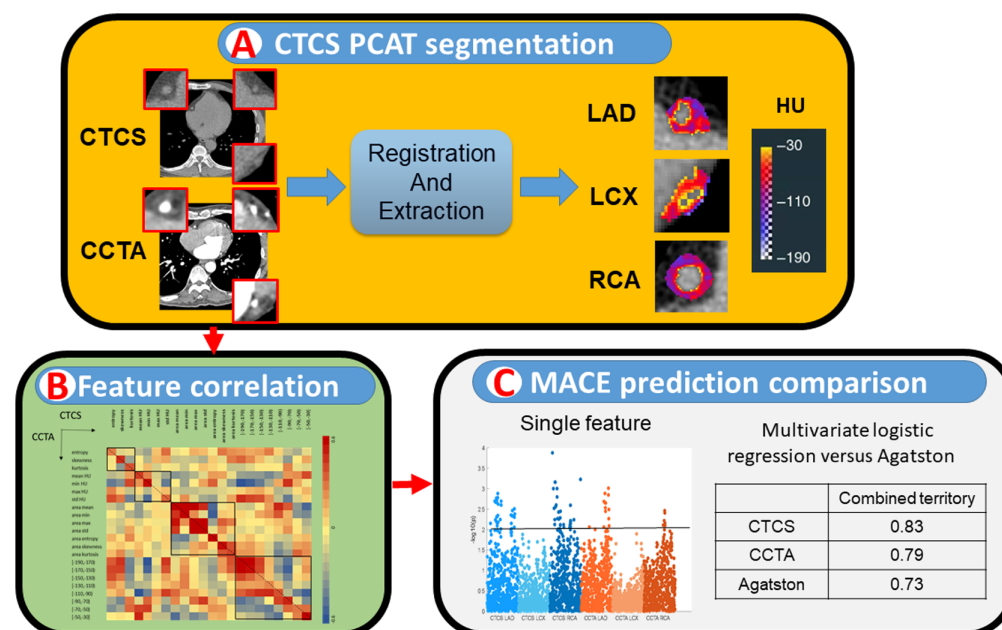


Fig. 1 Pipeline of PCAT analysis in CTCS images.

regions. After registration, masks for the main coronary arteries (LAD, LCX, and RCA) were transformed to corresponding locations in CTCS images.

We developed a novel axial-disk method for the analysis of PCAT rather than the more conventional curved multiplanar reformatting (MPR) to avoid the potential confound from interpolating thick (3 mm) image slices in CTCS. We created axial-disk-masks centered on the coronary artery center with two times the axial diameter of the first 40-mm segmented lumen, giving binary axial-disk masks. For RCA, we excluded the first 10-mm segment of the artery to avoid interference from the aortic wall. To ensure a reasonable PCAT size, the maximum diameter of the disk is limited to 8 mm. Following noise reduction with a 3×3 median filter, we apply the fat HU window $[-190, -30]$ to identify PCAT.

PCAT features were extracted from voxels within binary masks in CCTA and CTCS axial-disk regions. From PCAT, we extracted 22 hand-crafted and 536 radiomics library (Pyradiomics¹⁶) features. For hand-crafted features, we focused on the HU histogram feature of PCAT HU values (e.g., small histogram, skewness, and kurtosis of the HU value histogram) and the PCAT axial area features (e.g., min and max area of PCAT in the axial disk). For radiomic features, we extracted (1) shape features such as surface volume ratio and major axis length, (2) texture features such as gray-level co-occurrence matrix, gray-level dependence matrix, gray-level run-length matrix, and neighborhood gray-tone difference matrix, among many that have been used in CCTA analysis.^{11,17,18} Texture features were calculated using PCAT voxels with 16 bins of discretization. Radiomics were extracted at both original PCAT images and after three-dimensional wavelet transformation. Wavelet transformation decomposes the data into high and low-frequency components, enabling capturing discontinuities, ruptures and singularities, and coarse structure of the data.

As registration quality was important to the pipeline, we evaluated registration quality visually and quantitatively. To quantify registration results, we manually segmented coronary arteries in CTCS images and compared results with the registered arteries from CCTA. Distance errors were assessed by the average distance between the centers of the axial disks in registered coronary artery masks originating from CCTA and the manually segmented ones from CTCS.

2.3 Machine Learning and Statistical Analyses

For both CCTA and CTCS images, we determined the relative importance of various PCAT features and made MACE predictions. We compared the same features in paired CTCS (contrast-free) and CCTA (with iodine contrast) using Spearman's rho correlation. We used univariate logistic regression to generate *p*-values for each hand-crafted and radiomic feature in Manhattan plots. Bonferroni correction to reduce false positives was applied to features by dividing the significance level of $\alpha = 0.05$ by the number of components that described 99.5% of the radiomic variation.¹⁹ We used multivariate logistic regression and five-fold cross-validation to build MACE predictive models and compared the area under the receiver operating characteristic curves (AUC) to assess performance on testing data. To reduce redundancy, we excluded features with a correlation coefficient >0.7 . In addition, we created a combined model using a bagging strategy that takes the maximum probability of all three coronary arteries.

3 Results

Registration accuracy was sufficient to enable the identification of PCAT regions in CTCS images (Fig. 2). Across patients, the average distance between the centers of the axial disks generated in CCTA and registered to CTCS was only 1.36 ± 0.78 mm from those manually marked in CTCS images. This is comparable to the size of a voxel ($0.4 \text{ mm} \times 0.4 \text{ mm} \times 3 \text{ mm}$ voxels). As PCAT is segmented using the fat-window thresholds within relatively large axial disks (<8 -mm diameter), this uncertainty is deemed acceptable.

Streak artifacts characteristic of beam hardening and/or motion were commonly observed in the CCTA PCAT regions (Fig. 3). Compared with these artifact-containing CCTA images, CTCS images were homogeneous in the PCAT region. Images devoid of iodine have greatly reduced beam hardening due to the absence of iodine in the ventricle and reduced motion artifacts due to the absence of high-contrast moving objects.

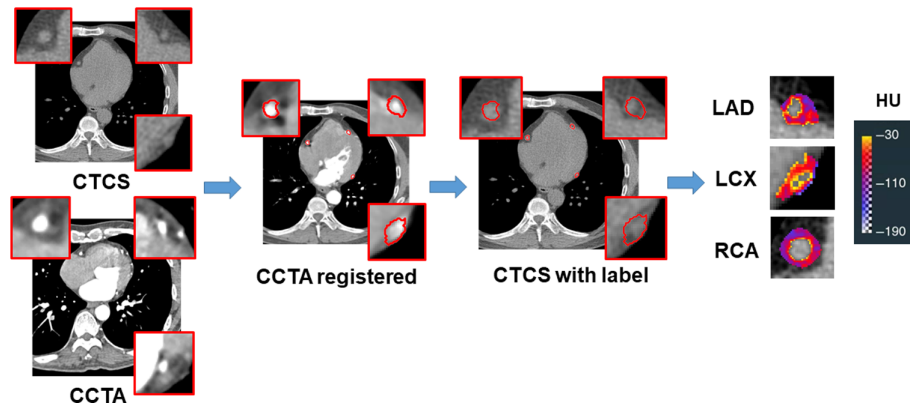


Fig. 2 Segment coronary arteries in CTCS using registration results in CCTA. After registering CCTA images to CTCS images, CCTA semi-automatic coronary artery segmentation was deformed (shown as red contours) and copied to CTCS. We could see registered segmentations aligned well with image evidence in CTCS. After applying the “axial-disk” method, we were able to assess PCAT in non-contrast CTCS images.

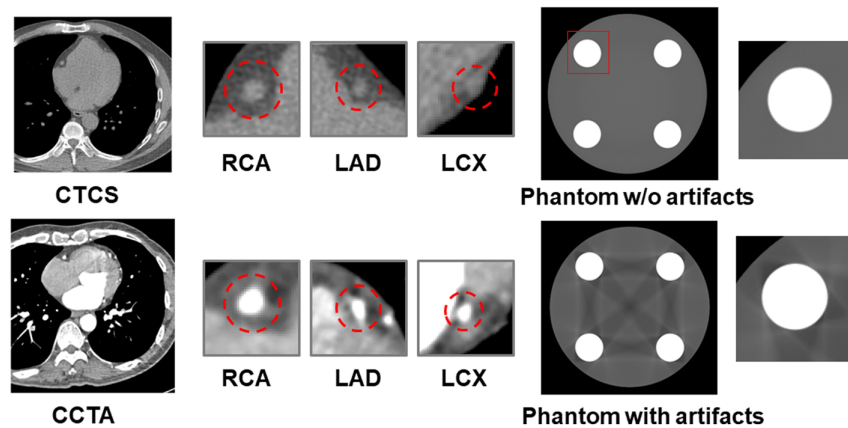


Fig. 3 Artifacts in CCTA PCAT greatly affect PCAT features. The upper ones are the CTCS image and its corresponding PCAT candidate regions, whereas the lower ones are for CCTA. In zoomed images, red dashed circles are the candidate regions before applying the fat threshold. We could observe streaking artifacts in CCTA PCAT candidate regions, but they were non-existent in homogeneous CTCS images without iodine in the coronaries and ventricular cavity to give beam hardening and accentuate motion artifacts. We plotted the original phantom mono-energetic (upper) and poly-energetic reconstruction which shows beam hardening artifacts (lower). The zoomed phantom images are from the upper left insert (red rectangle, 110 HU), and the one with beam hardening artifact showed similarity to CCTA zoomed PCAT regions.

In Table 2, for both CTCS and CCTA, we collected territory-specific mean HU and volumes for MACE and no-MACE patient groups. The analysis of the mean HU and volumes in the MACE group revealed slightly higher values in CTCS/CCTA scans, with respective mean differences of 3.19/1.15 HU and 0.46/0.2 cm³. It is noteworthy that these differences were positive and comparable in both CTCS and CCTA images.

We extracted and analyzed our own hand-crafted features and library radiomic features from PCAT in CTCS and CCTA images. CTCS PCAT features outperformed those from CCTA, with more features deemed discriminative based on all conventional and Bonferroni-adjusted significance levels (Figs. 4 and 6). We observed good Spearman’s rho correlation in “axial area” features (mean rho = 0.61) between CTCS and CCTA, indicating that CTCS could achieve similar PCAT morphology compared with CCTA (Fig. 5). Notably, there was also correlation in mean HU and the probability of being in the most elevated HU histogram bin [−50 HU, −30 HU],

Table 2 Comparison in PCAT mean HU and volume in MACE and no-MACE groups. We observed a slightly higher mean HU value in the MACE group in both CTCS and CCTA for three territories. A similar trend was observed as the MACE group had larger PCAT volumes.

		Mean HU		Volume (cm ³)	
		MACE	No MACE	MACE	No MACE
CTCS	LAD	-70.3 ± 4.3	-73.5 ± 7.5	2.9 ± 0.8	2.5 ± 0.9
	LCX	-67.6 ± 5.8	-74.3 ± 6.4	3.7 ± 1.3	3.2 ± 1.2
	RCA	-70.0 ± 4.4	-70.3 ± 6.5	1.6 ± 0.4	1.4 ± 0.5
CCTA	LAD	-70.0 ± 3.6	-71.6 ± 7.2	3.2 ± 0.8	3.0 ± 1.0
	LCX	-69.7 ± 3.2	-71.9 ± 6.6	4.1 ± 0.8	3.7 ± 1.1
	RCA	-71.5 ± 5.4	-71.7 ± 8.4	2.1 ± 0.6	2.0 ± 0.8

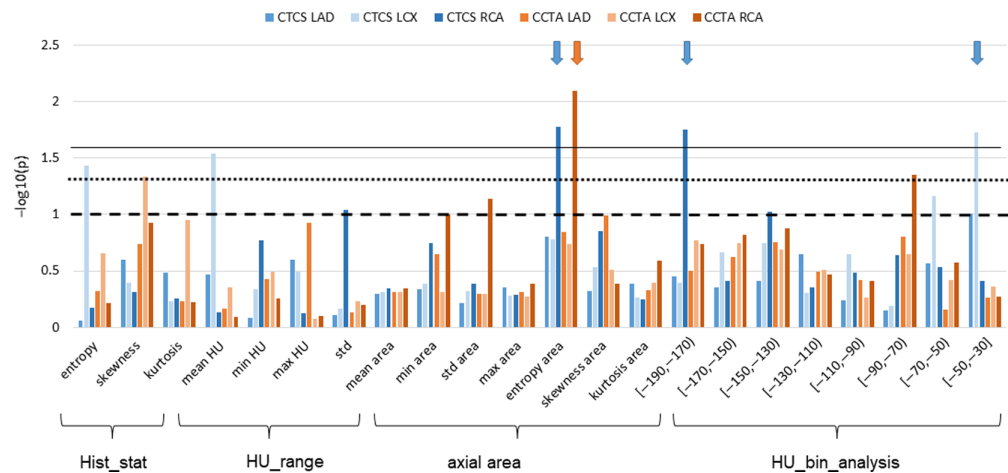


Fig. 4 MACE informative hand-crafted PCAT features from CCTA and CTCS. In three coronaries, we extracted 22 features (three histogram statistics, four histograms, seven PCAT areas in axial slices, and eight probability in ranges of HU values). Univariate logistic regression on MACE and no MACE groups gave *p*-values. The dashed, dotted, and solid lines represent *p* = 0.1, *p* = 0.05, and the Bonferroni-adjusted significance level for *p* = 0.05 (giving *p* = 0.025), respectively. By raising the threshold to *p* = 0.1, we can ensure the identification of discriminative features by limiting the number of false negatives. CTCS (blue)/CCTA (orange) gave 9/5, 5/3, and 3/1, for *p* equal to 0.1, 0.05, and 0.025, respectively. In all cases, the numbers of CTCS features deemed discriminative exceeded those of CCTA.

the bin presumably most related to PCAT inflammation. We further investigated the best 20 CCTA PCAT library radiomic features and examined their correlation with measurements from CTCS images (Fig. 6). We found that “wavelet intensity radiomics” showed a good correlation between CTCS and CCTA, whereas “wavelet texture radiomics” showed poorer correlation (Fig. 7). By employing a multivariable logistic model and incorporating hand-crafted features, we assessed the predictive capability for determining MACE (Figs. 8 and 9). Distinctly, the CTCS AUC was better than that for CCTA, although we cannot reliably reject the null hypothesis of no difference (*p* = 0.57). Nevertheless, this preliminary result suggests that CTCS may be as good or better than CCTA for this analysis. In addition, although the CTCS PCAT fat features are quite different than coronary calcifications giving direct assessment of atherosclerosis, MACE prediction from CTCS PCAT was comparable to that for Agatston score, suggesting good promise. Interestingly, when we combined PCAT hand-crafted and radiomic library features from CTCS, the AUC was slightly degraded (0.83 to 0.77), but this anomaly was insignificant.

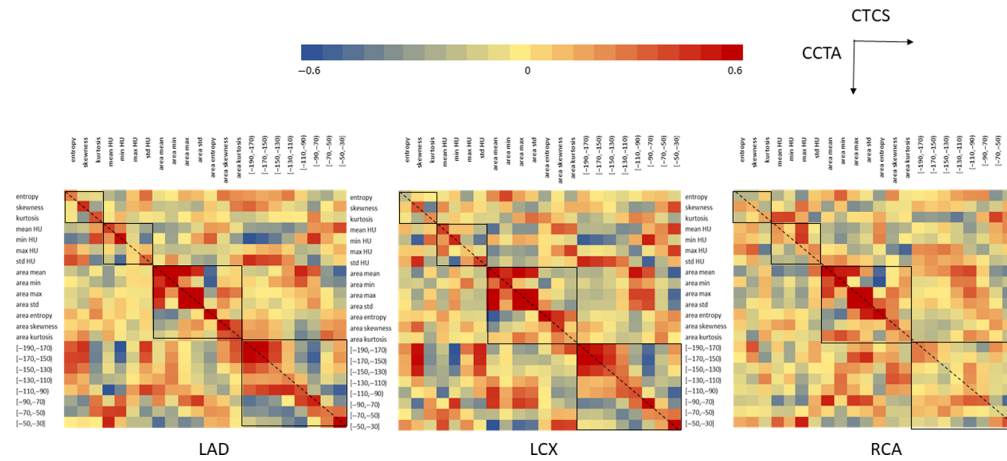


Fig. 5 Correlation of PCAT features from CTCS and CCTA images. The orders for CTCS and CCTA PCAT features are the same in Spearman's rho heatmaps of three coronary arteries, the diagonal dashed line shows the correlation of the same feature across image modalities, and boxes stand for each feature category derived from manual clustering. The best correlations were in the “axial area” category, showing that CTCS could catch similar PCAT morphology compared with CCTA.

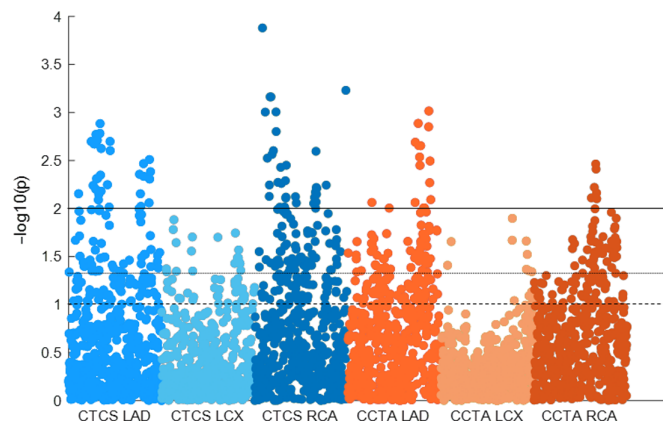


Fig. 6 CTCS PCAT radiomics performed better than CCTA. We extracted 536 radiomic features on each coronary artery. CTCS (blue)/CCTA (orange) gave 341/256, 203/137, and 63/22, for p equal to 0.1, 0.05, and 0.01, respectively. In all cases, the numbers of CTCS features deemed discriminative exceeded those of CCTA, indicating that CTCS PCAT features can achieve comparable performance compared with CCTA ones.

4 Discussion and Conclusion

In this study, we investigated the feasibility of utilizing non-contrast CTCS images for PCAT assessment. Some of the main findings follow. Registration with CCTA images enabled, for the first time, the identification of PCAT regions from CTCS images from all three major coronary arteries. The univariate analysis provided a number of promising features from CTCS images for MACE prediction that actually exceeded the number in paired CCTA images. Some hand-crafted features and radiomics library features showed a correlation between CTCS and CCTA. For the prediction of MACE, CTCS PCAT features slightly outperformed features from CCTA, albeit not in a significant way with our limited paired dataset. CTCS PCAT analysis exhibits comparable or near-comparable performance to that of CCTA. Taken together, results suggest promise in PCAT analysis from CTCS images.

Using our processing pipeline, we were able to automatically localize PCAT in three major coronary arteries in CTCS images. Existing studies on non-contrast images have extracted PCAT assessments using manual segmentation of the RCA artery.^{20,21} The registration error was small

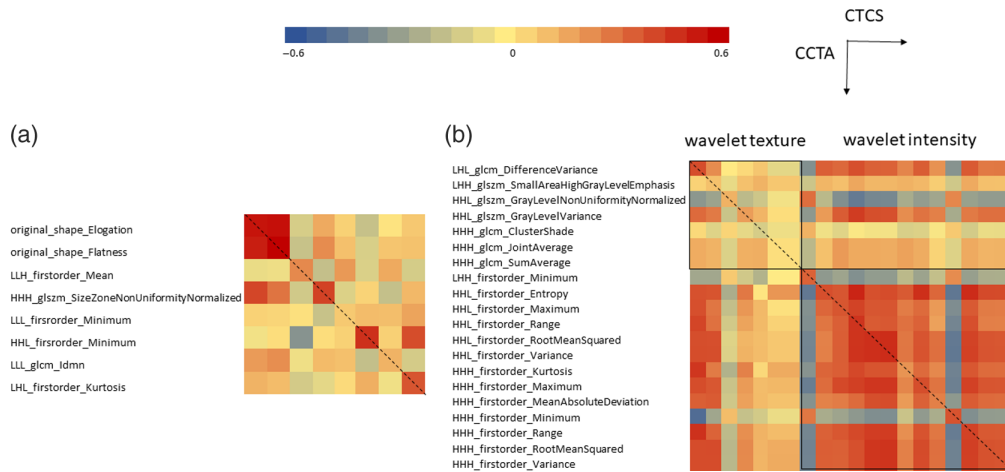


Fig. 7 PCAT radiomic correlation in CTCS and CCTA. We take LAD for example, panel (a) shows left in Spearman's rho heatmap of reported good CCTA PCAT features in CTCS and CCTA, and panel (b) is the best 20 CCTA PCAT radiomics in our study and its correlation to CTCS. The diagonal dashed line shows the correlation of the same feature across image modalities and boxes stand for each feature category. We observed shape-related radiomics in panel (a) were highly correlated, and wavelet intensity radiomics in panel (b) were well correlated across image modalities, showing CTCS could catch similar PCAT morphology compared with CCTA. However, wavelet texture radiomics of CCTA PCAT were not similar to CTCS ones, which can be visually seen in Fig. 2.

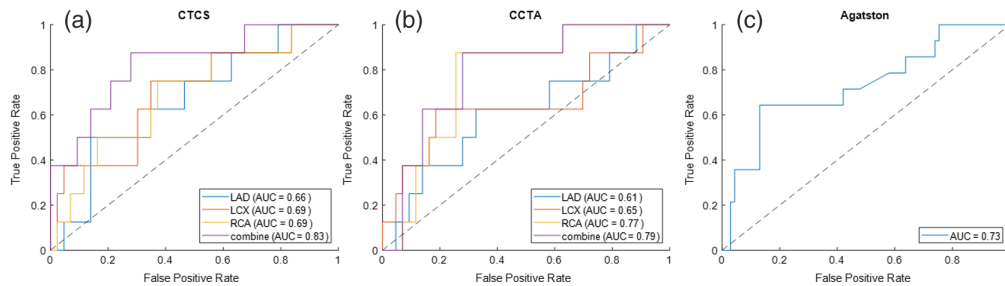


Fig. 8 Prediction of MACE from PCAT handcrafted features extracted from CTCS and CCTA images. For CTCS, we show MACE prediction for features from individual arteries and for a combined multi-instance method where we take the maximum probability of MACE from each artery for a patient (a). In panel (b), we present a similar figure for CCTA. In panel (c), we show MACE prediction for the Agatston score. The multi-instance combined model gave the best result. In terms of best AUCs in each panel, CTCS, CCTA, and Agatston gave 0.83, 0.79, and 0.73, with no statistical difference between them.

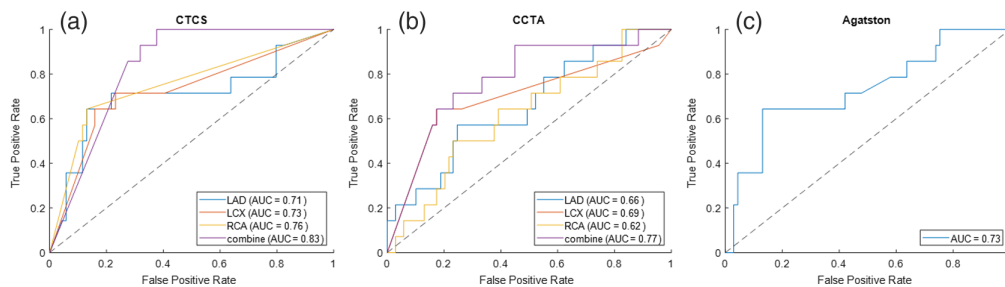


Fig. 9 Prediction of MACE from PCAT radiomic features extracted from CTCS and CCTA images. For CTCS, we show MACE prediction for a combined multi-instance method from each artery performed best (a). In panel (b), we present a similar figure for CCTA. In panel (c), we show MACE prediction for the Agatston score. In terms of best AUCs in each panel, CTCS, CCTA, and Agatston gave similar performances with no statistical difference between them.

(~1.4 mm), comparable to voxel sizes (Fig. 2). Registration quality was deemed sufficient to segment PCAT. Because axial disks tended to be about 6 mm in diameter, small displacements of the axial disk center would have a small effect on results. In fact, when we evaluated PCAT RCA volumes from CTCS images using our pipeline, we found good agreement (Dice score 0.83 ± 0.11 , $N = 5$) with that from manual identification of the vessel center. As argued previously, a curved MPR PCAT analysis common for 0.75-mm-thick CCTA images would be inappropriate for 3-mm-thick CTCS images, due to extreme oversampling of voxels in regions of high vessel curvature. We consider the axial-disk method the most appropriate alternative.

Regarding PCAT, there are notable differences between CTCS and CCTA, which may favor using CTCS. In a previous report using CT cardiac perfusion imaging,¹⁴ we identified the presence of iodine perfusion in PCAT and demonstrated changes in PCAT HUs, apparent volumes, and radiomics due to the presence of the iodine bolus in PCAT. This could represent a major confounding factor in CCTA images across individuals due to individual hemodynamic and CCTA acquisition time. In addition, beam hardening and motion artifacts prevalent in CCTA images could further result in marked image artifacts that may degrade the quality of CCTA images for PCAT evaluation (Fig. 3). The non-contrast CTCS images have much more homogenous PCAT regions. These issues pose major advantages of CTCS over CCTA.

Regardless of their differences, the trends observed in PCAT assessment were consistent between CTCS and CCTA. In both CTCS and CCTA images, we observed higher mean HU values and larger volume of PCAT are likely to associate with MACE (Fig. 4), similar to previous reports.^{22,23} In addition, interesting PCAT intensity features such as mean HU and PCAT HU range $[-50, -30]$ showed a good correlation between CTCS and CCTA. Similarly, we also found a good correlation between CCTA and CTCS for MACE informative shape elongation and mean value after three-dimensional wavelet transformation. We believe CTCS could serve as an alternative method to study PCAT since assessments are in good correlation.

For both CCTA and CTCS PCAT radiomic studies, we found features extracted after wavelet transformation are more informative than ones from the original image [Fig. 7(b)]. The literature supports the usefulness of wavelet features in CCTA, indicating a possible correlation to fibrosis and vascularity, reflecting permanent changes in adipose tissue induced by chronic coronary inflammation.^{11,24,25} Interestingly, wavelet features in non-contrast CTCS were also predictive, perhaps suggesting this to be a finding worthy of more investigation.

The principal limitation of this study is the limited sample size. The size was limited due to the difficulty in registering data and identifying PCAT regions in CTCS images. Nevertheless, this preliminary study is most promising suggesting that it will be a worthy endeavor to develop means for automatic analysis of PCAT in CTCS images.

In conclusion, our study demonstrates that CTCS images can be used to analyze PCAT and that PCAT assessments in CTCS might be as valuable for predicting cardiovascular risk prediction as those from CCTA. Importantly, CTCS images do not suffer from the confounds found in CCTA images due to the presence of iodine. Given the low cost and prevalence of CTCS images, additional studies of PCAT in CTCS images are warranted. For future work, we plan to develop a more automated pipeline to address challenges such as the reliance on human involvement, leveraging advanced machine learning and deep learning techniques to enhance efficiency and accuracy.

5 Clinical Perspective

PCAT attenuation, as evaluated in CT angiography, has been linked to fat inflammation, CAD, and cardiovascular risk. Our study reveals the feasibility and advantage of assessing PCAT from non-contrast CT calcium score (CTCS) images, with extracted features that can predict MACE. CTCS images are not hindered by the presence of iodine and artifacts found in CT angiography images. Results suggest that screening, low-cost CTCS images could be an alternative for the assessment of PCAT. Future studies are required to validate the generalizability of our findings, which hold promise for enhancing protocols in assessing cardiovascular risk.

Disclosures

The only potential conflicts of interest relevant to the technology described herein are pending Case Western Reserve University (CWRU) and University Hospital (UH) patents to analyze CT calcium score images. Unrelated to the technology described herein, Case Western Reserve University has licensed cardiac CT perfusion analysis technology to BioInVision, Inc. David L. Wilson is part owner of BioInVision, Inc. This information has been disclosed to Case Western Reserve University, and David L. Wilson has an approved CWRU plan for managing potential conflicts of interest.

Code and Data Availability

The code developed for this study is available upon reasonable request from the corresponding author. Due to confidentiality agreements and data protection policies, the clinical data utilized in this research, acquired at Mackay Memorial Hospital, Taiwan, are not publicly available. Access to these data is restricted and governed by the regulations of the institution. Researchers interested in accessing the data must seek approval directly from Mackay Memorial Hospital and adhere to their data sharing protocols.

Acknowledgments

This research was supported by the National Heart, Lung, and Blood Institute (Grant Nos. R01HL167199, R01HL165218, R01 HL143484, and R44HL156811). This research was conducted in a space renovated using funds from an NIH construction (Grant No. C06 RR12463) awarded to Case Western Reserve University. The content of this report is solely the responsibility of the authors and does not necessarily represent the official views of the National Institutes of Health. The grants were obtained via collaboration between Case Western Reserve University, University Hospitals Cleveland Medical Center, and Mackay Memorial Hospital. This work made use of the High-Performance Computing Resource in the Core Facility for Advanced Research Computing at Case Western Reserve University. The veracity guarantor, Hao Wu, affirms to the best of his knowledge that all aspects of this paper are accurate.

References

1. M. J. Budoff and K. M. Gul, "Expert review on coronary calcium," *Vasc. Health Risk Manage.* **4**(2), 315–324 (2008).
2. H. S. Hecht, "Coronary artery calcium scanning: the key to the primary prevention of coronary artery disease," *Endocrinol. Metab. Clin. North Amer.* **43**(4), 893–911 (2014).
3. M. J. Blaha et al., "Providing evidence for subclinical CVD in risk assessment," *Glob. Heart* **11**(3), 275–285 (2016).
4. A. Hoori et al., "Enhancing cardiovascular risk prediction through AI-enabled calcium-omics," arXiv:2308.12224 (2023).
5. A. Hoori et al., "An enriched survival study of epicardial adipose tissues risk on major adverse cardiovascular event in CT calcium score images," *Proc. SPIE* **12468**, 124680T (2023).
6. S. N. Verhagen and F. L. J. Visseren, "Perivascular adipose tissue as a cause of atherosclerosis," *Atherosclerosis* **214**(1), 3–10 (2011).
7. H.-Y. Lee, J.-P. Després, and K. K. Koh, "Perivascular adipose tissue in the pathogenesis of cardiovascular disease," *Atherosclerosis* **230**(2), 177–184 (2013).
8. H. W. Kim et al., "Perivascular adipose tissue and vascular perturbation/atherosclerosis," *Arterioscl. Thromb. Vasc. Biol.* **40**(11), 2569–2576 (2020).
9. M. Konishi et al., "Pericardial fat inflammation correlates with coronary artery disease," *Atherosclerosis* **213**(2), 649–655 (2010).
10. A. S. Antonopoulos et al., "Detecting human coronary inflammation by imaging perivascular fat," *Sci. Transl. Med.* **9**(398), eaal2658 (2017).
11. E. K. Oikonomou et al., "A novel machine learning-derived radiotranscriptomic signature of perivascular fat improves cardiac risk prediction using coronary CT angiography," *Eur. Heart J.* **40**(43), 3529–3543 (2019).
12. J. Shang et al., "Prediction of acute coronary syndrome within 3 years using radiomics signature of pericoronary adipose tissue based on coronary computed tomography angiography," *Eur. Radiol.* **32**, 1256–1266 (2021).
13. S. Almeida et al., "Feasibility of measuring pericoronary fat from precontrast scans: effect of iodinated contrast on pericoronary fat attenuation," *J. Cardiovasc. Comput. Tomogr.* **14**(6), 490–494 (2020).
14. H. Wu et al., "Cardiac CT perfusion imaging of pericoronary adipose tissue (PCAT) highlights potential confounds in coronary CTA," arXiv:2306.15593 (2023).

15. M. P. Heinrich et al., "MRF-based deformable registration and ventilation estimation of lung CT," *IEEE Trans. Med. Imaging* **32**(7), 1239–1248 (2013).
16. J. J. van Griethuysen et al., "Computational radiomics system to decode the radiographic phenotype," *Cancer Res.* **77**(21), e104–e107 (2017).
17. Lin Andrew et al., "Myocardial infarction associates with a distinct pericoronary adipose tissue radiomic phenotype," *JACC: Cardiovasc. Imaging* **13**(11), 2371–2383 (2020).
18. M. Kolossváry et al., "Contribution of risk factors to the development of coronary atherosclerosis as confirmed via coronary CT angiography: a longitudinal radiomics-based study," *Radiology* **299**(1), 97–106 (2021).
19. X. Gao, J. Starmer, and E. R. Martin, "A multiple testing correction method for genetic association studies using correlated single nucleotide polymorphisms," *Genet. Epidemiol.* **32**(4), 361–369 (2008).
20. X.-Y. Jiang et al., "Non-contrast CT-based radiomic signature of pericoronary adipose tissue for screening non-calcified plaque," *Phys. Med. Biol.* **67**(10), 105004 (2022).
21. D. Takahashi et al., "Validation and clinical impact of novel pericoronary adipose tissue measurement on ECG-gated non-contrast chest CT," *Atherosclerosis* **370**, 18–24 (2023).
22. A. A. Mahabadi et al., "Association of pericoronary fat volume with atherosclerotic plaque burden in the underlying coronary artery: a segment analysis," *Atherosclerosis* **211**(1), 195–199 (2010).
23. M. S. Sagris et al., "Pericoronary adipose tissue attenuation index (FAI) – a new imaging biomarker and its diagnostic and prognostic utility: a systematic review and meta-analysis," *Eur. Heart J.* **42**(Supplement_1), ehab724.0197 (2021).
24. J. Wl, "Value of pericoronary adipose tissue texture analysis in diagnosis of coronary artery disease," *BJSTR* **35**(5), 28009–28015 (2021).
25. D. Wen et al., "Influence of different segmentations on the diagnostic performance of pericoronary adipose tissue," *Front. Cardiovasc. Med.* **9**, 773524 (2022).

Biographies of the authors are not available.